

Electrical Impedance Tomographic Shape Sensing for Soft Robots

Wenci Xin^{ID}, Graduate Student Member, IEEE, Fangmeng Zhu^{ID}, Peiyi Wang^{ID}, Graduate Student Member, IEEE, Zhexin Xie^{ID}, Zhiqiang Tang^{ID}, Member, IEEE, and Cecilia Laschi^{ID}, Fellow, IEEE

Abstract—With infinite degrees of freedom, soft robots are expected to achieve dexterous and complex tasks, but this also puts forward higher requirements for their sensing capabilities. An important sensing task in soft robots is sensing their own deformation and current shape. Currently, most of the existing soft shaping sensors are limited by local perception abilities, stretchability, and fabrication difficulties. We propose a sensing method based on Electrical Impedance Tomography (EIT), which reconstructs conductivity patterns distributed on a surface, by considering the deformation-caused resistance changes. Comparison between the theoretical and experimental patterns reveals that even though the quality of the pattern is affected by a large amount of noise, the considered features are still able to reflect the change of shape. With the help of neural networks, the pattern is decoded to the physical data related to the deformation. Detection of the planar shape changes and proprioception of a sensor-integrated soft robot are presented to exhibit the capability of our method. Results show that the detected error ratios are mostly under 5% and 3% for 2D and 3D conditions respectively.

Index Terms—Soft robotics, soft sensors and actuators, electrical impedance tomography, proprioceptive sensing.

I. INTRODUCTION

IN SOFT robots, proprioceptive shape sensing is one of the essential sensing tasks, given the importance of the deformability of their bodies [1]. Shape sensing is needed for soft robots to detect their configuration, which is helpful for control of movements and interaction with the environment. Shape sensing systems in literature mostly employ an array of sensors to reconstruct the robot's deformation, such as strain gauges [2], accelerometers [3] and magnetic transducers [4]. Some authors tried to reduce the number of sensors by morphologically optimizing the design and constructing the shape using learning

Manuscript received 4 September 2022; accepted 19 January 2023. Date of publication 27 January 2023; date of current version 6 February 2023. This letter was recommended for publication by Associate Editor C. Cao and Editor Y.-L. Park upon evaluation of the reviewers' comments. This work was supported in part by NUS startup Grant ‘RoboLife,’ in part by MOE Tier 2 Grant ‘REBOT,’ in part by the National Robotics Program, Singapore, through Soft and Hybrid Phase 2a Project, and in part by the National Research Foundation, Singapore, through its Medium Sized Centre Programme - Centre for Advanced Robotics Technology Innovation (CARTIN). (Corresponding author: Wenci Xin.)

Wenci Xin, Fangmeng Zhu, Zhexin Xie, Zhiqiang Tang, and Cecilia Laschi are with the Department of Mechanical Engineering, National University of Singapore, Singapore 117575 (e-mail: wxin@u.nus.edu; axellezhu@gmail.com; zhexinxie@buaa.edu.cn; zq.tang@nus.edu.sg; mpeclc@nus.edu.sg).

Peiyi Wang is with the Robotics Research Center, Beijing Jiaotong University, Beijing 100044, China (e-mail: wpy342423@163.com).

This letter has supplementary downloadable material available at <https://doi.org/10.1109/LRA.2023.3240368>, provided by the authors.

Digital Object Identifier 10.1109/LRA.2023.3240368

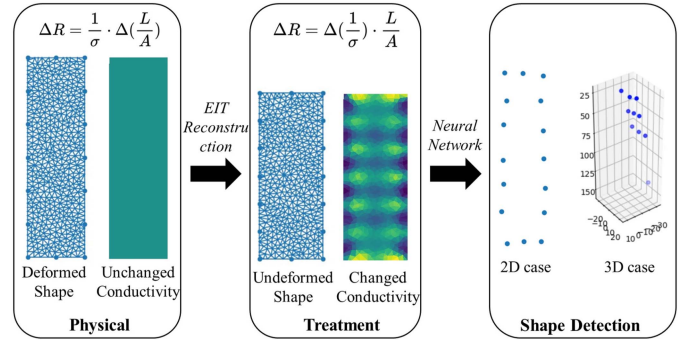


Fig. 1. Overview of the task-oriented EIT shape sensing method.

methods [5], [6], or pairing the sensor feedbacks with geometrical models [7], [8], [9]. However, the sparse discrete information of sensors limits these sensing methods, hard to have a high spatial sensing density. Meanwhile, model-based methods require the robot to maintain specific geometries, which usually conflict with their deformability. Since continuous estimation provides nearly infinite information about the desired deformation, it is considered one of the solutions to overcome these drawbacks. Recent works are focusing on forecasting the continuous shape change by processing different types of signals via statistical features, like diffuse optical waves [10], Bragg gratings [11], piezoelectricity [12] and vision [13]. Nonetheless, because of the usage of inextensible optical fibers and materials, as well as deformation-caused obstructions, these sensing methods can only endure a very limited stretch. By setting the optical fiber as a helical configuration, this limitation is reduced [14], but bulky generated data and high cost still restrict the application of these methods.

Electrical Impedance Tomography (EIT) is a technique that uses measured voltages, when injecting currents between a number of electrodes placed around an area, to reconstruct the impedance distribution inside the entire area. It works with a wide range of materials and tissues. Since such a technique could easily distinguish different organs and tissues with diverse impedance, it has been employed as a non-invasive real-time medical monitoring method for years [15]. Although EIT has well-known disadvantages concerning the quality of its reconstructed image, which is poor because based on an ill-posed problem, it is now gradually improved with the help of neural networks [16], [17], [18]. Since Nagakubo et al. tried to implement EIT in touch sensing in 2007 [19], EIT has also attracted

the attention of the robotics community for its application in human-robot interaction [20]. By combining two fabric layers with different conductivity and detecting the impedance change, Park and his colleagues developed a large-area tactile sensor with learning-based signal processing [21] and multimodal perception [22]. Judd et al. proposed a low output dimensionality skin sensor [23]. Besides touch sensing, Zhang et al. also employed EIT for hand gesture recognition via monitoring the impedance changing of wrist muscle groups [24]. However, there are few studies on the shape sensing of robots, especially with the large deformations of soft robots. The main reason is that the unknown electrode positions make the contour of the sensor unknowable and then the inverse problem insoluble [25]. Only Avery et al. utilized a frequency division multiplexed EIT system by means of conductive liquids to sense the bending angle of a variable stiffness soft robot [26], but higher dimensional deformation studies like planar deformation are still missing.

We propose an EIT shape sensing method in this letter. We aim at measuring the deformation of the EIT sensor surface when stretched along the lateral (longitudinal and transversal) directions. Fig. 1 shows the scheme of the strategy. To avoid the impedance changing and deformation simultaneously affecting the EIT output, the sensor is made of unitary material. Based on Pouillet's law, this ensures all the resistant variation comes from the shape change of the sensor. Then, these variations are regarded as equivalent to the internal conductivity change with non-deformation, and do the EIT reconstruction. Finally, by means of neural networks training by specific task data, the shape of the sensor in 2D or 3D space is reconstructed. Our system is then task-oriented.

The main contributions of this work include:

- developed an EIT-based continuous shape sensor that is stretchable
- proposed a data processing strategy to overcome the influence of unknown electrode positions for EIT reconstruction
- presented the feasible application of the shape sensor in both 2D and 3D conditions

The paper contents are organized as follows: Section II introduces the design and fabrication of the shape sensor; Section III presents the theoretical model and the simulation for shape sensing; experiments are detailed in Section IV, while corresponding results and analysis are provided in Section V; Section VI draws conclusions on the results and discusses future works.

II. DESIGN & FABRICATION OF SHAPE SENSOR

To ensure the sensor is effective for a soft robot and is easily integrated, the sensor should be stretchable, internally conductive, with low contacting resistance, easily fabricated, and robust. Fig. 2(a) shows our design. The sensor is embedded in silicone as a layer of conductive material and the electrodes are distributed along the perimeter. Multi-walled carbon nanotube (MWCNT) is selected as the conductive material because of its high resistance and low price. However, the MWCNTs tend to adhere to copper, and create gaps when being stretched, which can disrupt the connection of copper electrodes. To solve the issue, liquid metal is employed as the linking medium due to its

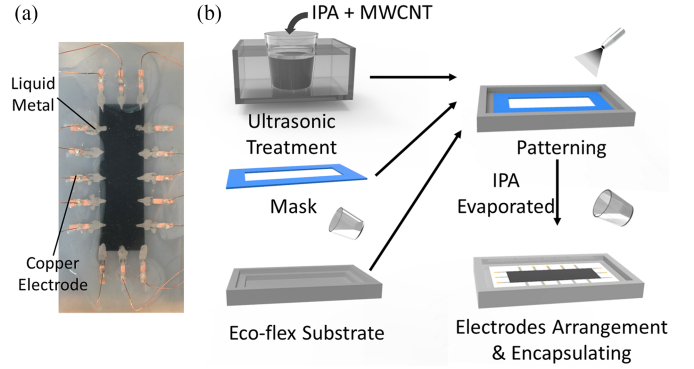


Fig. 2. (a) Design and (b) fabrication process of the shape sensor.

mobility and low resistance. The shape of the sensor depends on the task, and a rectangular sensor with a dimension of 60 mm × 20 mm is presented as an example here.

Details of the sensor fabrication process are exhibited in Fig. 2(b). Firstly, the MWCNTs are diffused in the isopropanol (IPA) using the ultrasonic treatment for 40 minutes with a weight ratio of 2%. During the treatment, a one-time used mask is prepared, and the substrate is molded using degassed silicone mixture Eco-flex 0030. Then, the suspension of the treated fluids is deposited through the assembled mask to do the pattern by spray gun. After removing the mask, the mixed IPA evaporates under a circumstance of 65 °C. Last but not least, the step of arranging electrodes, connecting them to the sensing area using liquid metal manually, and encapsulating the sensor with another batch of silicone are carried out.

III. THEORETICAL FORMULATION & SIMULATION

In the reconstruction process of EIT, two types of problems are involved: forward problem and inverse problem. These two problems are defined by the solving direction between the boundary voltages and conductivity distribution. To simulate the proposed shape sensing method, these problems need to be successively solved. These calculations are achieved based on public library pyEIT [27]. Details are described in this section.

A. Forward Problem

For the sensing area Ω with a smooth boundary $\partial\Omega$, the conductivity distribution σ is a function of spatial variable x . In our condition, by using the direct current, the magnet field of the Maxwell equations is neglected. Thus, for the sensing area, the continuum Kirchoff's law holds as:

$$\nabla \cdot (\sigma \nabla \phi) = 0 \text{ in } \Omega \quad (1)$$

where ϕ denotes the electric potential. From Ohm's Law, the current density J could also be expressed by the electrical potential as:

$$J = -\sigma \nabla \phi \quad (2)$$

such that the current density on the boundary j is:

$$j = -J \cdot n = \sigma \nabla \phi \cdot n \quad (3)$$

where n represents the normal vector of the boundary $\partial\Omega$. This is a Dirichlet-Neumann boundary value problem, and the potential ϕ is uniquely determined with given conductivity σ and current density j . In simple cases, equations are easily calculated, whereas the area is discretized and solved by the finite element method (FEM) in general cases, and it takes the form of:

$$A\phi = I \quad (4)$$

where A is a $N \times N$ symmetric matrix that is called global stiffness matrix, $\phi = (\phi_1, \dots, \phi_N)$ is the vector composed of potential values at each element vertex, and I consists of zeros except for vertices where current flows. Specifically, +1 and -1 denote current flowing in and out separately.

To calculate the forward problem, the Jacobian matrix which is derivative of voltages with respect to conductivity is required. Denoting V_{dm} as the m th voltage measurement under d th current injection, the variation of it is:

$$\delta V_{dm} = - \int_{\Omega} \delta\sigma \nabla \phi_d \cdot \nabla \phi_m dS \quad (5)$$

Then, as the conductivity of the sensor is discretized to elements with a constant value in the FEM method, the Jacobian matrix is given by:

$$\mathbf{J}_{dm,k} = \frac{\partial V_{dm}}{\partial \sigma_k} = - \int_{\Omega_k} \nabla \phi_d \cdot \nabla \phi_m dS \quad (6)$$

B. Inverse Problem

According to the previous derivation, considering the physical measurement's noise n , the forward problem has been linearized as:

$$\Delta V = \mathbf{J}(\sigma) \Delta \sigma + n \quad (7)$$

Since the dimension of the conductivity is much larger than the voltage measurements, the Jacobian matrix is irreversible. Instead, the one-step Gauss-Newton (GN) reconstruction method [28], which is widely used in the EIT field, is exploited. As a result, the approximated variety of the conductivity $\Delta\hat{\sigma}$ is:

$$\Delta\hat{\sigma} = (\mathbf{J}^T W \mathbf{J} + \lambda^2 R)^{-1} \mathbf{J}^T W V = H \Delta V \quad (8)$$

where H is the inverse Jacobian matrix, R is the regularization matrix, W is the covariance of the noises which is simplified to be the identity matrix, and λ is the hyperparameter that adjusts the trade-off between resolution and noise attenuation in the reconstruction. Instead of directly assigning it as an identity matrix, R is defined to be a diagonal matrix in which $R_{ii} = (\mathbf{J}^T \mathbf{J})_{ii}^p$, where p is another designed hyperparameter describing the compromise between the pushing noise to the boundary or center.

C. Simulation

A comparison between two sets of patterns helped assess the difference between the theoretical derivation in simulation and experimental results. Fig. 3 shows the details. Three types of conditions are examined including elongation, transversal

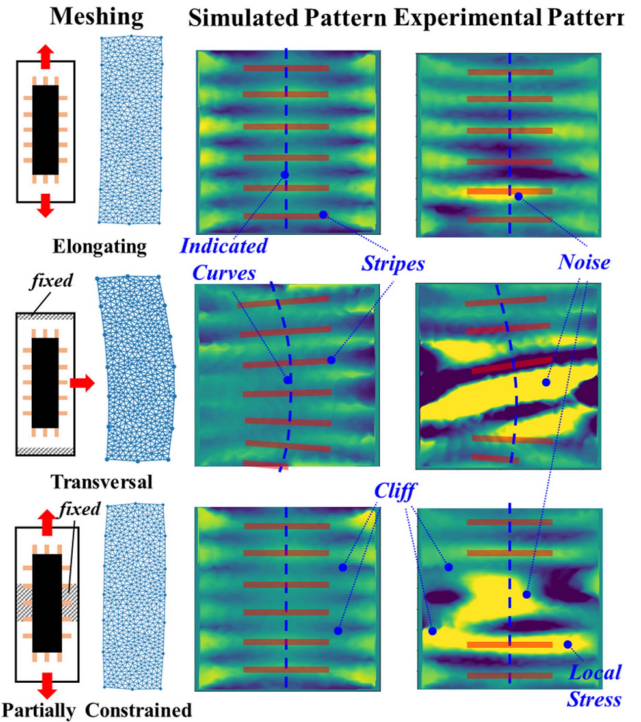


Fig. 3. Feature comparison between the simulated pattern (linear interpolated) and experimental pattern (linear interpolated) under different conditions. (Red bars: Stripes; Blue dash lines: Indicated curves).

stretch, and partially constrained stretch. Here, all of the patterns have been linearly interpolated for better presentation.

Although noise in the experimental pattern submerges a lot of valuable information, it is still very clear that two sets of patterns (simulated and experimental) exhibit similar features. Firstly, stripes appear in the form of alternated light and dark, and the color at the position of electrodes indicates the general deformation of the sensor, with light indicating elongation and dark indicating contraction in the vertical direction. According to the Poisson effect, neglecting the deformation of thickness, the elongation in one direction makes the other contract, so that stretching the sensor horizontally generates the same pattern as vertical contraction, which makes the transversal stretching pattern occupied with dark stripes. Secondly, the distribution of the stripes indicates the shape of the deformed sensor. As the impedance change is caused by the deformation, similar changes could then be regarded as similar deformation. Since the stripe is a combination of similar impedance, its arrangement then reflects the shape of the deformation. As the labels in Fig. 3 show, red bars are the direction of stripes, and blue dash lines are smooth curves connecting these stripes. Though some of the stripes in the latter two conditions are blocked by the noise, a very similar curve to the physical deformation still could be generated with existing stripes. Thirdly, since the intensity of the pattern shows the magnitude of deformation, there should be a cliff of intensity for adjacent areas with different deformation. This feature is even more pronounced for the partially stretched case, since the middle part is constrained with little deformation. In addition, due to the assembly error,

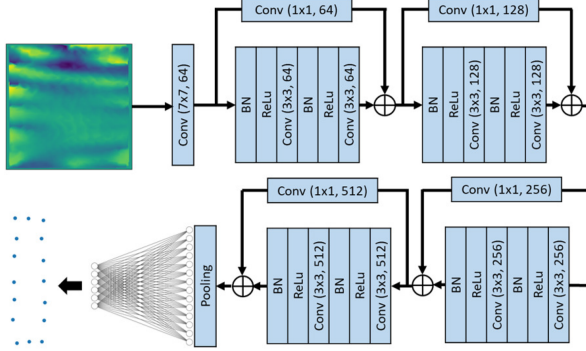


Fig. 4. Designed Network Structure.

the margin of the constraining pad applies undesired local stress to the sensor. The local stress locates at the cliff area, which on the other hand verifies the correctness of the cliff indication.

Even though the theoretical derivation is complete, the presence of a large noise limits the application of an analytical solution. Alternatively, as similar features exist in both theoretical and experimental patterns, the latter has a strong correlation with the deformation. Thus, a neural network is employed to extract the features and match them to the sensor deformation.

IV. EXPERIMENT SETTINGS

A. Training Settings

Due to the large amount of data generated by one EIT reconstruction, the convolutional neural network ResNet18 [29] is employed to save computational resources. To represent the shape of the sensor, electrodes' positions are set as the output of the network. Fig. 4 shows the revised structure of the employed network. A fully connected layer is applied after the residual convolutional layers to revise the network as a regression solver. However, since the positions of the discretized elements are non-grid-like, they cannot be directly computed as tensors for convolution. As a solution, the reconstruction results are linearly interpolated to a 224×224 matrix. Alternatively, directly inputting the reconstructed pattern as a figure using color information would work, while the changing threshold of the colorbar and the larger amount of the parameters in the network make this scheme abandoned.

Empirically, the coordinate values of positions are normalized via selecting a reference point and dividing by the original dimension, and the parameters of the training process have been carefully tuned. In detail, the dataset is divided into batches with a size of 64, and the loss function is selected to use mean absolute error (MAE) with weighted factors to emphasize the importance of different electrodes. Adam optimizer is employed to do the optimization with a learning rate of $1e^{-6}$ and a weighted decay of 0.001.

B. Planar Deformation Settings

To test the performance of our proposed method, a group of planar deformation sensing tasks is designed. These tasks are set the same as the simulation conditions, which include stretching

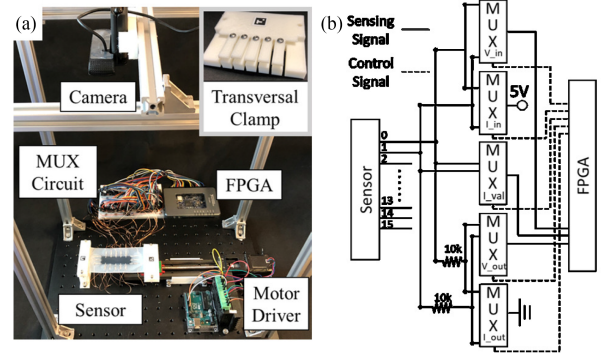


Fig. 5. Experimental settings of the planar shape sensing experiments (a) Hardware configuration (b) Multiplexer circuit.

the sensor longitudinally, transversely, and with constraints. Fig. 5(a) shows the schematic of the experimental configurations. The sensor is fixed by two 3D printed clamps, one of which is connected to a leading screw driven by the motor. For lateral stretching, the clamps are designed with separate sub-clamps. Such a design facilitates point stretching of large deformations, rather than overall deformations like what longitudinal stretching does. Besides, to test the response of the proposed method for local deformation, a 3D printed pad is adhered to the sensor from below using silicone epoxy in the third situation. Deformation of the confined area will then be limited greatly compared to the original status.

As EIT reconstruction requires rapid injection of currents and collection of voltages, the data acquisition system should be able to switch between electrodes and process data quickly. Since FPGA has perfect parallel computing capability and high sampling rate, it is used as the solution in this work, and multiplexers (MUXs) are used for switching. Meanwhile, because the injection and measurement should occur simultaneously, two independent circuits containing the sensor are required with electrode switching capability. Accordingly, a MUX circuit is designed as Fig. 5(b) shows. Within the circuit, five MUX (CD4051BE, Texas Instruments Inc.) are connected to every electrode, two for the voltage measurement and the rest for injecting the current. In the measuring circuit, a $10\text{ k}\Omega$ resistor is inserted for the purpose of protection, and two ends of the circuit are connected to the FPGA (myRIO1900, National Instruments Ltd.) to measure the potential difference. For the injecting circuit, the protecting resistor is used as the sampling resistor. The voltage divider of this sampling resistor reflects the value of injected current and consequently overcomes the defect that the FPGA card cannot directly generate current. To prevent the influence of MUX's current leakage, three MUXs are embedded in the circuit connecting to the power supply, ground, and sampling resistor respectively. During the process, the sampling MUX and ground MUX are always switched to the same electrode, and the sampling rate is set to 5 Hz.

C. Spacial Surface Recognition Settings

Besides 2D circumstances, the implementation of the proposed sensing method in 3D space has also been tested.

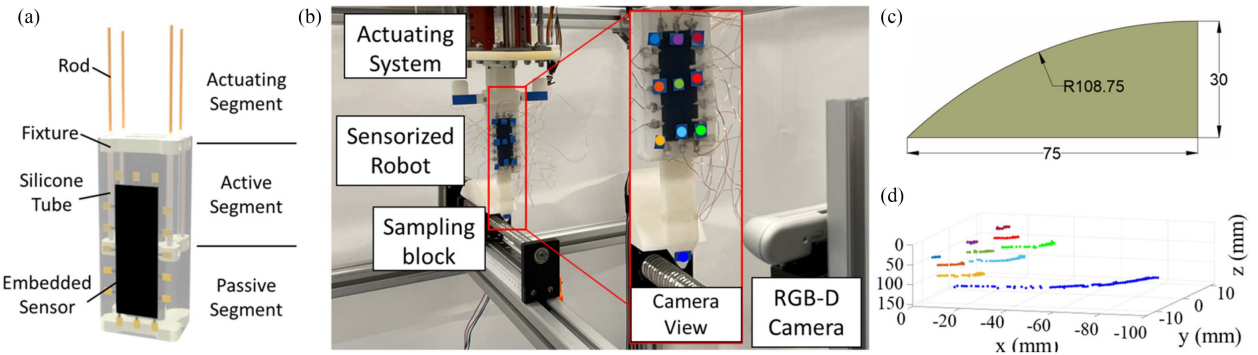


Fig. 6. Experimental settings of the spacial shape sensing experiments. (a) Design of the proprioceptive soft robot (b) Data collection experiment setup (c) Dimension of the sampling block (d) Plots of the collected data.

A sensorized soft robot is designed and fabricated, whose schematic is shown in Fig. 6(a). The robot includes three segments that are separately used for actuation, active deformation, and passive deformation. Four superelastic shape memory alloy rods are inserted into half of the silicone-made robot body. To reduce the friction between rods and the silicone body, silicone tubes are employed to hold the internal part of the rods. Three fixture pads are embedded in the robot, two of which are on the top and bottom and one at the end of the rods. An EIT sensor is made on one of the surfaces with the fabrication method described in Section II. Particularly, the sensor is divided equally by the middle fixture, such that the sensor could recognize the active and passive deformations with the same capability. Moreover, a hollow structure is designed from top to bottom through the robot. Such a design on the one hand helps to locate the intermediate fixture during the manufacturing process, and on the other hand enables the robot to attach different end effectors.

Fig. 6(b) shows the setup of the experiment. A 3D printed probe is attached to the bottom of the robot, and the sensor is expected to capture the shape of the surface as it passes through the probe. By means of a connector, the robot is mounted on the actuating system introduced in [30]. By pushing and pulling the rod, the robot could be elongated, shortened, and bent. Twelve color markers are placed among the system to collect training data, and an RGB-D camera (RealSense D435, Intel Inc.) is employed to recognize their spacial positions.

To enrich the diversity of data, the experiment is designed in two sessions. Firstly, by solving the constant curvature (CC) model, the robot actively bends up for around 40 degrees with multiple sampling points. Secondly, it is passively deformed as the surface block moves forward and shifts the probe. The dimension of the sampling surface is presented in Fig. 6(c), which is half of a convex surface with a length of 75 mm and a height of 30 mm. Fig. 6(d) exhibits the collected data, which clearly shows the movement of the robot during the process of the data collection.

V. RESULTS & DISCUSSION

A. Planar Stretching

Based on the settings described in the previous section, training data are first collected aiming at three different tasks. For

each task, the network is trained for 20 epochs using 200 pairs of data, 90% of which is used for training and the rest for testing. During the physical test, a red marker is stuck to the corner of the sensor to locate the reference electrode point.

Results of the experiment are exhibited in Fig. 7, which includes states of the sensor at the beginning, midpoint, and end and the corresponding EIT reconstructed pattern. Considering the stroke, the stretching distance is proportionally set to be 20 mm, 10 mm, and 15 mm respectively. The complete sensor performances during the process are provided in the supplied videos. In the figure, red dots are the electrode positions detected by the sensor based on the EIT pattern. During the process, the reference potential for the calculation of equation (8) is set the same as the one used for reconstructing the dataset. Thus, patterns also exist for unstretched states due to the noises and fluctuating signals. For the overall elongating stretch, light and dark stripes appear gradually as the stretch progresses, and the contrast increases at the same time. The rule of these stripes obviously follows those conclusions from the simulating patterns, which they locate horizontally and the magnitude becomes larger.

For the other two stretches, the patterns are influenced a lot by the noises. The initial patterns of these two conditions are nearly the same, which might be caused by the contacting resistance changes during the assembling. Even though the details of the pattern are visually hidden by the outliers, effective information is still stored within the reconstructed matrix and recognized by the proposed method. By adjusting the threshold of the colorbar, masked features are manifested as the experimental patterns presented in Fig. 3. In terms of the partially constrained stretch experiment, demarcation lines that partition the confined area and the elongated area appear, and become significant with the stretching going on. Different from the lateral condition, the bright spots created by the noise here do not change during the process because the corresponding area in the sensor is not deformed. At the bottom of the confined relevant area enclosed in the pattern, there is a horizontal bright stripe. Instead of being created by the deformation, such a phenomenon is caused by the interaction between the sensor and the constraining pad. With the progress of elongation, the width of the sensor decreases, which contradicts the fixation of the pad. Stress is then applied to the sensor through the edge of the pad and shifts the resistance

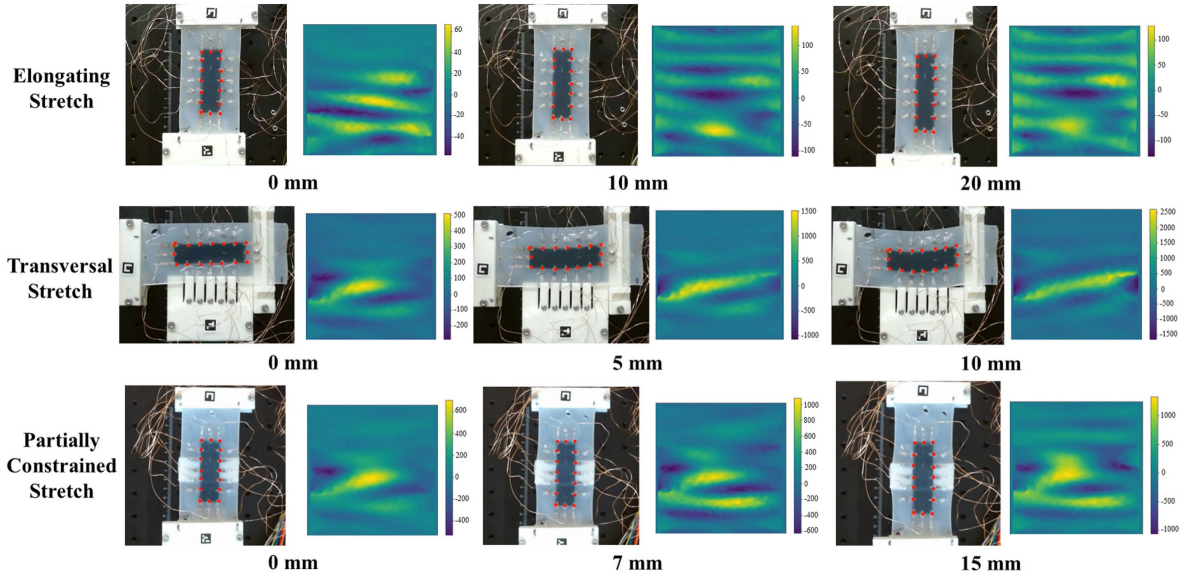


Fig. 7. Performance of the shape sensing method under three different conditions and their corresponding reconstructed patterns (Red dots: detected positions output by the sensor).

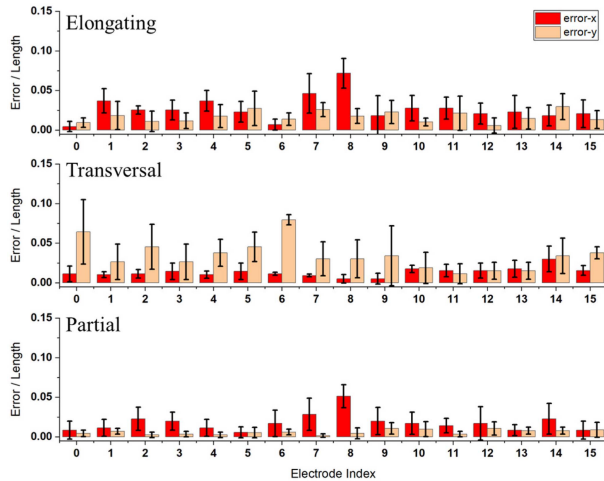


Fig. 8. Errors of the electrode positions detection through the experiment.

of the area. As a result, a line-like local deformation pattern is added to the EIT reconstruction pattern.

Fig. 8 shows the errors of our EIT-based shape sensing method during the process. The 16 electrodes are numbered clockwise from 0 to 15 with reference to the electrode in the lower left corner when the sensor is placed vertically. Generally, errors are mostly less than 5% of the original dimension, and the partial deformation performs the best with mostly less than 3%. Errors in the direction of longer edges are larger than the other. For two elongation conditions, the largest error occurs at the 8th electrode, which is the distal end relative to the reference one. This is reasonable as it has the largest coordinate value. As for the lateral stretch condition, errors concentrate on the long side of the depression. Since the error that should be zero at electrode 0 still has a large value and variance, this phenomenon is doubted caused by the low-quality recognition of the positioning marker, and shift the detected point away from the actual position.

In addition, we tested the mechanical influence of integrating the sensing layer, by recording the forces required to stretch two samples with and without the sensing layer. Results show that the equivalent stiffness of these two samples is 0.079 N/mm and 0.084 N/mm respectively. Such a 0.005 N/mm difference will not significantly affect any mechanical properties of the host robot, which in other words is promising for the general applicability of the sensor.

B. Surface Recognition

Since the goal of the task is to recognize the shape of the surface through passive deformation of the robot, the data is trained on a targeted basis. Except for the calibration markers on the connector, all marker points on the robot are set as the output of the network. Particularly, the influence of the probe tip position in the training loss function has been doubled to emphasize its importance. After a process of 30 epochs, the network is utilized to recognize the shape of an unknown surface, whose dimension is presented at the left of Fig. 9(c).

Due to the limitation of the stroke of the moving platform, the waving surface is tested from both ends, which correspond to convex and concave surfaces respectively. Fig. 9 shows details of the process and results. As mentioned earlier, the process includes two stages of active and passive deformation, and four types of states are involved. In detail, the sensor stays at the idle status waiting for the activating signals, and bending is from the robot active deformation by pulling the rods. During the contacting period, the robot experiences pushing given by the testing block. Since the height of the probe tip is lower than the edge of the block, its body will touch and be tangent to the block first. Once the tip rises to the surface of the block, it begins to follow its shape, which is the period of interest. Fig. 9(b) exhibits the complete record of the sensed height of the probe tip during the experiment. Initially, the robot does not

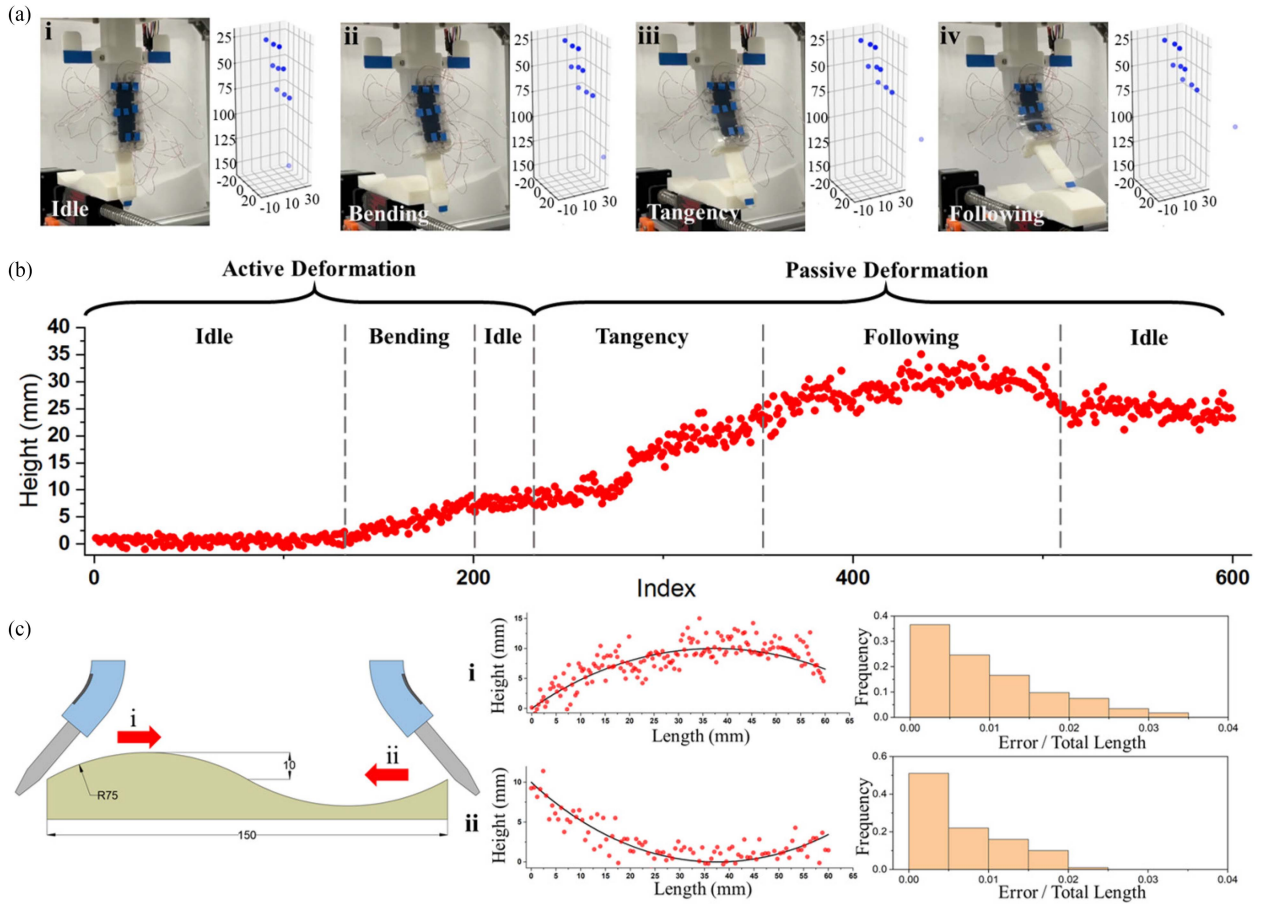


Fig. 9. Process and results of the surface recognition. (a) Figures and corresponding sensor detection for the status of i) Idle ii) Bending iii) Tangency and iv) Following (b) Recorded sensing heights of detecting probe tip point during the experiment (c) Schematic of the experiment and sensing results (Comparison with the ground truth and data distribution) from two side.

have any motions and the height of its tip stays around a specific value, which performs as a horizontal line in the figure. Then, the active bending makes the tip through an arcuate trajectory. An idle period occurs again as the robot is waiting for the testing block moving forward. Next, passive deformation starts, the tip is continuously lifted in the period of tangency, and the shape information of the surface is captured via the following motion of the probe. Finally, when the mobile platform reaches the end of the lead screw, it stops moving, which causes the tip to stop at a fixed point.

Fig. 9(c) shows the comparison between the collected data and the ground truth of the waving surfaces and their statistical distribution. According to the influence of noises, fluctuations occur among the detected points, but within a small threshold. Overall, the errors are less than ± 2 mm. Considering the ratio of the error, errors are mostly within 3% of the robot's total length, and better in the concave situation. For both two surfaces, over 60% of the detecting error are less than 1%.

VI. CONCLUSION

In this letter, we present an EIT-based shape sensing method for soft robots. By considering the deformation-caused resistance changes as the variation of internal conductivity with

no deformation, deformed information is encoded as the EIT reconstructed pattern. The fabrication method of a low-cost and easily integrated MWCNT-based shape sensor has also been introduced. By means of theoretical derivation, simulations are completed by solving the EIT forward and inverse problem in succession. The comparison of simulated and experimental patterns shows a strong similarity in pattern features even under a large influence of noise.

With the help of neural networks, deformed information is decoded. Two sets of experiments including planar deformation and surface recognition in stereo space are utilized to examine the performance of our method. Corresponding hardware platforms and algorithms are built to collect the data of focused tasks and do the verification. As a result, the detection errors are mostly less than 5% and 3% for the two tasks respectively.

Although the proposed shape sensing method can successfully detect the deformation, it still has limitations that need to be improved. During the experiments, signals of the deformation are significant with a 0.5 mm stretch or 3 mm radius hemisphere, but the noises limit the application of precise detection. The 60% device stretchability also limits the usage of the method. Improving the signal quality and device stretchability through the improvement of the fabrication, electrode arrangement, and

signal processing method are two urgent problems. In addition, the current EIT pattern structure is 2D, which limits the diversity of sensed deformations and is troubled by conformal deformations [31]. Introducing the proposed method to three-dimensional meshed deformation is one of the solutions, as well as the next development. Our method is task-oriented, and requires collecting the specific task data before being used. In the future, with the usage of simulation-generated data, a universal pre-trained network that only needs few data for calibration can be developed.

ACKNOWLEDGMENT

The authors would like to thank Mr. Kunhao Zheng for his fruitful suggestions on neural network training and tuning.

REFERENCES

- [1] B. Shih et al., “Electronic skins and machine learning for intelligent soft robots,” *Sci. Robot.*, vol. 5, no. 41, 2020, Art. no. eaaz9239.
- [2] L. A. Garcia-Garcia, G. Valsamakis, P. Kreitmair, N. Munzenrieder, and D. Roggen, “Inferring complex textile shape from an integrated carbon black-infused ecoflex-based bend and stretch sensor array,” in *Proc. Adjunct ACM Int. Joint Conf. Pervasive Ubiquitous Comput. Proc. ACM Int. Symp. Wearable Comput.*, Virtual USA, 2021, pp. 298–303.
- [3] P. Mittendorfer and G. Cheng, “3D surface reconstruction for robotic body parts with artificial skins,” in *Proc. IEEE/RSJ Int. Conf. Intell. Robots Syst.*, 2012, pp. 4505–4510.
- [4] A. Hermanis, R. Cacurs, and M. Greitans, “Acceleration and magnetic sensor network for shape sensing,” *IEEE Sensors J.*, vol. 16, no. 5, pp. 1271–1280, Mar. 2016.
- [5] T. G. Thuruthel, B. Shih, C. Laschi, and M. T. Tolley, “Soft robot perception using embedded soft sensors and recurrent neural networks,” *Sci. Robot.*, vol. 4, no. 26, 2019, Art. no. eaav1488.
- [6] O. Gläuser, D. Panozzo, O. Hilliges, and O. Sorkine-Hornung, “Deformation capture via soft and stretchable sensor arrays,” *ACM Trans. Graph.*, vol. 38, no. 2, pp. 1–16, 2019.
- [7] Y. Shapiro, G. Kósa, and A. Wolf, “Shape tracking of planar hyperflexible beams via embedded PVDF deflection sensors,” *IEEE/ASME Trans. Mechatron.*, vol. 19, no. 4, pp. 1260–1267, Aug. 2014.
- [8] H. A. Wurdemann et al., “Embedded electro-conductive yarn for shape sensing of soft robotic manipulators,” in *Proc. IEEE 37th Annu. Int. Conf. Eng. Med. Biol. Soc.* Milan, 2015, pp. 8026–8029.
- [9] J. W. Booth et al., “OmniSkins: Robotic skins that turn inanimate objects into multifunctional robots,” *Sci. Robot.*, vol. 3, no. 22, 2018, Art. no. eaat1853.
- [10] I. M. Van Meerbeek, C. M. De Sa, and R. F. Shepherd, “Soft optoelectronic sensory foams with proprioception,” *Sci. Robot.*, vol. 3, no. 24, 2018, Art. no. eaau2489.
- [11] T. L. T. Lun, K. Wang, J. D. L. Ho, K.-H. Lee, K. Y. Sze, and K.-W. Kwok, “Real-time surface shape sensing for soft and flexible structures using fiber Bragg gratings,” *IEEE Robot. Automat. Lett.*, vol. 4, no. 2, pp. 1454–1461, Apr. 2019.
- [12] C. Rendl et al., “FlexSense: A transparent self-sensing deformable surface,” in *Proc. 27th Annu. ACM Symp. User Interface Softw. Technol.*, Honolulu, Hawaii USA, 2014, pp. 129–138.
- [13] H. Sun, K. J. Kuchenbecker, and G. Martius, “A soft thumb-sized vision-based sensor with accurate all-round force perception,” *Nature Mach. Intell.*, vol. 4, no. 2, pp. 135–145, 2022. [Online]. Available: <https://rdcu.be/cHCl9>
- [14] K. C. Galloway, Y. Chen, E. Templeton, B. Rife, I. S. Godage, and E. J. Barth, “Fiber optic shape sensing for soft robotics,” *Soft Robot.*, vol. 6, no. 5, pp. 671–684, Oct. 2019.
- [15] I. Frerichs et al., “Chest electrical impedance tomography examination, data analysis, terminology, clinical use and recommendations: Consensus statement of the TRAnsational EIT developmeNt stuDy group,” *Thorax*, vol. 72, no. 1, pp. 83–93, 2017.
- [16] G. Ma, H. Chen, P. Wang, and X. Wang, “Multi-frame constrained block sparse Bayesian learning for flexible tactile sensing using electrical impedance tomography,” *IEEE Trans. Comput. Imag.*, vol. 8, pp. 438–448, 2022.
- [17] S. Liu, J. Jia, Y. D. Zhang, and Y. Yang, “Image reconstruction in electrical impedance tomography based on structure-aware sparse Bayesian learning,” *IEEE Trans. Med. Imag.*, vol. 37, no. 9, pp. 2090–2102, Sep. 2018.
- [18] Z. Wei and X. Chen, “Induced-current learning method for nonlinear reconstructions in electrical impedance tomography,” *IEEE Trans. Med. Imag.*, vol. 39, no. 5, pp. 1326–1334, May 2020.
- [19] A. Nagakubo, H. Alirezaei, and Y. Kuniyoshi, “A deformable and deformation sensitive tactile distribution sensor,” in *Proc. IEEE Int. Conf. Robot. Biomimetics*, 2007, pp. 1301–1308.
- [20] D. Silvera-Tawil, D. Rye, M. Soleimani, and M. Velonaki, “Electrical impedance tomography for artificial sensitive robotic skin: A review,” *IEEE Sensors J.*, vol. 15, no. 4, pp. 2001–2016, Apr. 2015.
- [21] H. Park, K. Park, S. Mo, and J. Kim, “Deep neural network based electrical impedance tomographic sensing methodology for large-area robotic tactile sensing,” *IEEE Trans. Robot.*, vol. 37, no. 5, pp. 1570–1583, Oct. 2021.
- [22] K. Park, H. Lee, K. J. Kuchenbecker, and J. Kim, “Adaptive optimal measurement algorithm for ERT-Based large-area tactile sensors,” *IEEE/ASME Trans. Mechatron.*, vol. 27, no. 1, pp. 304–314, Feb. 2022.
- [23] E. Judd, K. M. Digumarti, J. Rossiter, and H. Hauser, “NeatSkin: A discrete impedance tomography skin sensor,” in *Proc. IEEE 3rd Int. Conf. Soft Robot.*, 2020, pp. 33–38.
- [24] Y. Zhang, R. Xiao, and C. Harrison, “Advancing hand gesture recognition with high resolution electrical impedance tomography,” in *Proc. 29th Annu. Symp. User Interface Softw. Technol.*, Tokyo, Japan, 2016, pp. 843–850.
- [25] M. Soleimani, C. Gómez-Laberge, and A. Adler, “Imaging of conductivity changes and electrode movement in EIT,” *Physiol. Meas.*, vol. 27, no. 5, pp. S103–S113, 2006.
- [26] J. Avery, M. Runciman, A. Darzi, and G. P. Mylonas, “Shape sensing of variable stiffness soft robots using electrical impedance tomography,” in *Proc. Int. Conf. Robot. Automat.* Montreal, QC, Canada, 2019, pp. 9066–9072.
- [27] B. Liu et al., “pyEIT: A python based framework for electrical impedance tomography,” *SoftwareX*, vol. 7, pp. 304–308, 2018.
- [28] A. Adler, T. Dai, and W. R. Lionheart, “Temporal image reconstruction in electrical impedance tomography,” *Physiol. Meas.*, vol. 28, no. 7, 2007, Art. no. S1-S11.
- [29] K. He, X. Zhang, S. Ren, and J. Sun, “Deep residual learning for image recognition,” in *Proc. IEEE Conf. Comput. Vis. Pattern Recognit.*, 2016, pp. 770–778.
- [30] P. Wang, Z. Tang, W. Xin, Z. Xie, S. Guo, and C. Laschi, “Design and experimental characterization of a push-pull flexible rod-driven soft-bodied robot,” *IEEE Robot. Automat. Lett.*, vol. 7, no. 4, pp. 8933–8940, Oct. 2022.
- [31] A. Boyle, A. Adler, and W. R. B. Lionheart, “Shape deformation in two-dimensional electrical impedance tomography,” *IEEE Trans. Med. Imag.*, vol. 31, no. 12, pp. 2185–2193, Dec. 2012.